Thalamo-insular pathway regulates tic generation via motor-limbic crosstalk

Authors:

Hiroto Kuno,[1] Natsumi Tsuji,[1] Kenta Kobayashi, [2] Toru Takumi, [1] Yoshihisa Tachibana [1,3,*]

[1]Department of Physiology and Cell Biology, Kobe University Graduate School of Medicine, Kobe, Japan.

[2]Section of Viral Vector Development, National Institute for Physiological Sciences, Okazaki, Japan.

[3]Lead contact

*Correspondence: yoshi@med.kobe-u.ac.jp

Corresponding author:

Dr. Yoshihisa Tachibana

Department of Physiology and Cell Biology,

Kobe University Graduate School of Medicine, Kobe, Japan.

7-5-1 Kusunoki-cho, Chuo-ku, Kobe, Hyogo 650-0017, Japan

Phone: +81 78 382 5832

E-mail: yoshi@med.kobe-u.ac.jp

Research topic: Neuroscience

Type of article: Research Article

Total of 49 pages with 6 figures (Key resources table and 5 supplemental figures are shown in the Supplementary Materials)

Summary: 119 words

References: 70

Keywords: striatal disinhibition, intralaminar thalamic nuclei, insular cortex, movement disorder, Tourette syndrome

Highlights:

1. c-Fos activation occurs in both motor and limbic structures in a mouse tic model
2. Basal ganglia outputs are transmitted to insula via intralaminar thalamic nuclei
3. Chemogenetic inhibition of thalamo-insular pathway suppresses motor tics
4. Thalamo-insular inhibition diminishes tic-associated activity in primary motor cortex

In Brief:

Abnormal basal ganglia activity originating from striatum drives insular cortex dysfunction via intralaminar thalamic nuclei, and its inhibition suppresses tic-like behaviors, highlighting motor–limbic circuit pathology in tic disorders.

SUMMARY

Tic disorders accompanied by premonitory urges are the hallmark symptoms of Tourette syndrome (TS), but the neuronal mechanism remains unsolved. Here, we show that striatal disinhibition induces motor tics in mice. This model exhibits c-Fos activation in both motor and limbic structures, such as the insular cortex (IC). Viral tracing demonstrates that aberrant striatal activity is ultimately transmitted to the insular cortex via the intralaminar thalamic nuclei, a potential target of deep brain stimulation in TS patients. We further identify tic-associated activity in the IC as well as the primary motor cortex (M1). Chemogenetic inhibition of the thalamo-insular pathway suppresses M1 synchronization and alleviates tic-like behaviors. These findings reveal motor-limbic circuit dysfunction as a key mechanism underlying tic disorders.

INTRODUCTION

Motor and vocal tics are characterized by sudden, rapid, repetitive movements or involuntary vocalizations.[1] These symptoms are often preceded by an uncomfortable sensation, known as a premonitory urge, which is transiently relieved by tic expression.[2-5] Gilles de la Tourette syndrome (TS) is diagnosed by the presence of multiple motor tics and at least one vocal tic persisting for over a year,[1] and is frequently accompanied by comorbidities such as obsessive-compulsive disorder (OCD) and attention-deficit/hyperactivity disorder (ADHD).[6-8] TS typically begins in childhood, affecting approximately 0.3–1.0% of school-aged children.[1,9-12] While symptoms often improve during adolescence, they can persist or even worsen into adulthood.[1,6]

Current treatment strategies in TS patients include behavioral therapy, pharmacological agents, and, in severe cases, surgical interventions.[13] Despite extensive clinical characterization, however, the neuronal mechanisms driving tic generation remain incompletely understood. Accumulating evidence implicates dysfunction of the cortico-basal ganglia (BG)-thalamo-cortical (CBGTC) circuits in the pathophysiology of TS.[14] Microinjections of $GABA_A$ receptor antagonists into the sensorimotor striatum reliably induce motor tics in rats[15,16] and monkeys[17-19]. Notably, similar manipulations in the associative or limbic subdivisions of the monkey striatum produce distinct behavioral phenotypes: hyperactive and impulsive behaviors, resembling symptoms of ADHD, or stereotyped behavior, reminiscent of OCD, respectively.[19] These findings support the "striatal disinhibition hypothesis", which posits that local GABAergic deficits underlie the pathophysiology of TS symptoms. The striatum contains diverse subtypes of GABAergic interneurons: parvalbumin-, calretinin-, and neuropeptide Y-positive neurons.[20] Postmortem studies have revealed a selective reduction of striatal

GABAergic interneurons in TS patients.[21,22] In parallel, the "hyperactive dopamine hypothesis" also provides a compelling framework since pharmacological interventions with dopamine receptor antagonists (i.e., antipsychotics) are clinically effective in suppressing tic symptoms in TS patients.[6,13,23] However, intrastriatal administration of dopamine agonists in rodents induces stereotyped behaviors, rather than motor tics.[24] Taken together, these findings highlight that striatal disinhibition-based animal models offer a mechanistically relevant approach for investigating the neuronal circuits underlying tic generation.

Here, we report that striatal injection of bicuculline, a $GABA_A$ receptor antagonist, in mice activates both motor and limbic structures, including the insular cortex (IC). We identify a basal ganglia output pathway to the IC via the intralaminar thalamic nuclei (ITN), and demonstrate that chemogenetic inhibition of this pathway alleviates tic-like behaviors. These results reveal a motor-limbic circuit that contributes to tic generation.

RESULTS

Unilateral striatal bicuculline injection induces tic-like movements

We established a mouse model of motor tics by unilateral injection of a low dose of bicuculline, a $GABA_A$ receptor antagonist (0.2 μg/μl, 0.20 μl per injection), into the motor domain of the dorsal striatum (dSTR) in head-fixed mice (Figure 1). This paradigm recapitulates striatal disinhibition protocols (Figure S1A) previously shown to induce motor tics in rats[15,16] and monkeys[17-19]. To monitor the tic-associated cortical activity, we simultaneously recorded electroencephalogram (EEG) signals from the primary motor cortex (M1) ipsilateral to the injection site, along with electromyogram (EMG) activity from the contralateral triceps muscle (Figures 1A and S1B). Bicuculline injection into the dSTR produced somatotopically organized tic-like movements in the contralateral body parts, with affected regions varying along the dorsoventral striatal axis from forelimb to orofacial areas (Figure S1B and Video S1), as previously reported.[15,16] In this study, we targeted the striatal injection site (AP: 0.0 mm, ML: 2.7 mm, DV: 3.5 mm from the bregma; Figure 1B), which reliably induced tic-like movements predominantly in the contralateral forelimb and orofacial regions (Figure S1B and Video S1). EEG spikes in the M1 emerged prior to EMG bursts and kinematic acceleration of the corresponding body parts (Figure 1C-1E for the forelimb; S1C-S1E for the mouth). On average, spikes occurred 17.0 ± 3.7 ms before EMG bursts and 20.7 ± 2.5 ms before movement acceleration (mean ± S.D.).

We next examined the temporal dynamics of the tic-like phenotype over 40 min following injection. The number of tic events and EEG spikes peaked at 10–20 min, gradually declined after 25 min, and returned to baseline by 40 min (Figures 1F and 1G). The amplitude of EEG

spikes remained relatively stable, then progressively decreased thereafter (Figure 1H). EMG amplitude and the velocity of wrist and mouth movements, quantified in 10-min bins, showed robust increases up to 30 min post-injection, then attenuated markedly (Figures 1I and S1F). The overall intensity of tic-like movements peaked at 10–20 min and diminished substantially by 30–40 min (Figures 1J, 1K, and S1G). Non-tic-associated EEG spikes became more prominent after 35 min (Figures 1L and 1M). Thus, striatal disinhibition induced transient tic-like movements with a duration of ~40 min in this model.

To further investigate the causal relationship between motor cortical activity and tic-like movements following striatal disinhibition, we performed two-photon Ca^{2+} imaging in mice expressing GCaMP6f under the synapsin promoter in both superficial (layer 2/3) and deep (layer 5/6) neurons of the ipsilateral M1 (Figures S2A and S2B). Following bicuculline injection, M1 neurons exhibited temporally synchronized Ca^{2+} transients (Figures S2C and S2D; see also Video S2). To quantify this synchrony, we calculated Pearson's correlation coefficient (C.C.) between pairs of M1 neurons (Figure S2D), revealing a significant post-injection increase in both superficial and deep layers (Figure S2E). This suggests enhanced synchronous activity among excitatory neurons in the ipsilateral M1. We next analyzed the amplitude and frequency of Ca^{2+} events before and after injection. The mean amplitude significantly increased in deep-layer neurons, while no change in the superficial layer (Figure S2F). In contrast, Ca^{2+} event frequency significantly decreased in both layers following the injection (Figure S2G). Finally, we assessed the relationship between M1 activity and tic-like movements. The response probability of M1 Ca^{2+} transients aligned to tic onsets was significantly higher than that observed in shuffled datasets with randomly permuted tic timings (Figure S2H; see Star Methods for details). Taken together, these findings indicate that striatal disinhibition induces highly synchronized, time-locked activity in M1 neurons associated with

motor tics.

Tic-associated brain activation in motor and limbic structures

To identify brain regions engaged during tic expression, we performed c-Fos immunohistochemistry following unilateral striatal bicuculline injection (0.2 μg/μl, 0.20 μl; same dose as in preceding experiments). Mice were perfused 90 min after injection, and brain sections were processed for c-Fos staining (Figure 2A). c-Fos mapping revealed robust neuronal activation in multiple brain structures on the ipsilateral side to the injection site (Figures 2A-2C). In the cortex, strong c-Fos expression was observed in medial prefrontal regions (including cingulate, prelimbic, infralimbic, and dorsal peduncular cortices), the primary (M1) and secondary (M2) motor cortices, and the insular cortex (IC). Subcortical activation was evident in the basal ganglia nuclei, including the dSTR, globus pallidus (GP), and subthalamic nucleus (STN). Thalamic activation involved motor thalamus (ventral anterior [VA] and ventrolateral [VL]), sensory thalamus (ventral posterolateral [VPL], ventral posteromedial [VPM], and posterior [Po]), and rostral intralaminar thalamic nuclei (rITN; central medial [CM], paracentral [PC], and centrolateral [CL]). Beyond sensorimotor regions, limbic structures such as the amygdala and hypothalamus also displayed high levels of c-Fos expression. Thus, unilateral striatal disinhibition elicited widespread activation across sensorimotor and limbic circuits with strong ipsilateral dominance (Figure 2D).

Insular cortical activity is associated with tic generation

Given the widespread activation observed in tic generation, we next focused on the insular cortex (IC), since several studies have proposed the IC as a potential trigger site for tics and their preceding "urges".[25,26] Consistent with this, human imaging studies have reported IC

activation in TS patients.[27,28]

To monitor tic-related activity in the IC and M1 (the final output node of motor commands), we performed *in vivo* Ca^{2+} imaging using fiber photometry (Figures 3A and 3B). Optical fibers were implanted into the ipsilateral M1 and bilateral IC one week after viral injections of AAV1-Syn-GCaMP6f (Figure 3A). Following unilateral striatal disinhibition, robust Ca^{2+} transients were observed in the ipsilateral M1 and ipsilateral IC, time-locked to motor tics (Figure 3B and 3C). The contralateral IC also exhibited tic-associated activity (Figure 3B and 3C). Analysis of temporal dynamics revealed that tic-associated Ca^{2+} activity in the ipsilateral M1 and bilateral IC peaked at 10–20 min post-injection and gradually diminished thereafter (Figure 3D and 3E), paralleling the time course of tic-like movements and M1 EEG spikes (Figure 1F-1K, S1F, and S1G).

The intralaminar thalamic nuclei relay basal ganglia outputs to the insular cortex

We next investigated the neuronal pathway mediating IC activation following striatal disinhibition. To identify the outputs from the dSTR, we first injected AAV1-CAG-tdTomato into the dSTR (Figure 4A). Anterogradely axonal terminals were observed in the GP, entopeduncular nucleus (EP), and substantia nigra pars reticulata (SNr), but not in the IC or other cortical regions.

To confirm the absence of a direct dSTR-IC projection, we injected AAV2retro-CAGGS-EGFP into the rostrocaudally middle IC (Figure 4B). No retrogradely labeled neurons were found in the striatum or the other basal ganglia nuclei (GP, EP, STN, and SNr). Instead, labeled neurons were detected in the dorsomedial regions of thalamus (dmTh), including the rITN, paraventricular/intermediodorsal nuclei (PV/IMD), and mediodorsal nucleus (MD) (Figure 4B). Notably, thalamic structures classically receiving BG output, such as the motor thalamus

(ventromedial [VM], and ventral anterior [VA]/ventrolateral [VL]) and parafascicular nucleus (Pf),[29-31] contributed minimally to IC-projecting neurons.

Because the SNr is the largest BG output nucleus in rodents,[31] we hypothesized that SNr neurons reach the IC via the dmTh. A large proportion of SNr neurons are parvalbumin (PV)-positive and exhibit projections similar to VGAT-positive neurons,[31,32] indicating that they are GABAergic projection neurons. We injected AAV1-FLEX-tdTomato into the SNr of PV-Cre mice (Figure S4E), revealing widespread projections to multiple thalamic regions, including the dmTh (Figures 4D and S4).

To test whether dmTh-projecting SNr neurons connect with IC-projecting dmTh neurons, we performed triple viral injections: 1) AAV2retro-CAGGS-Cre in the dmTh, 2) AAV1-FLEX-tdTomato into the SNr, and 3) AAV2retro-CAGGS-EGFP into the IC (Figure 4E). SNr axon terminals were apposed to IC-projecting dmTh neurons, particularly within the rITN.

These findings indicate that the IC receives BG outputs via the intralaminar thalamic nuclei, known targets of deep brain stimulation (DBS) in TS patients[33,34].

Chemogenetic inhibition of thalamo-insular pathway alleviates tic-like movements

To determine whether the thalamo-insular pathway contributes to motor tic generation, we tested whether tic-like movements induced by striatal disinhibition were attenuated by artificial inhibition of this pathway using designer receptors exclusively activated by designer drugs (DREADD).

As an initial step, we examined whether direct inhibition of the IC reduced tic expression. AAV8-hSyn-hM4Di-mCherry was bilaterally injected into three rostrocaudally distinct sites of the IC (Figures 5A and 5C). Thirty minutes after intraperitoneal administration of either vehicle or clozapine-N-oxide (CNO; DREADD agonist), bicuculline was repeatedly injected into the

same dSTR site via a guide cannula. To control for repeated injection effects, the sequence was vehicle (1st test), CNO (2nd test), and vehicle (3rd test) (Figure 5E). Tic severity was quantified during the 30-min period following bicuculline injection, when tics were prominent, by measuring the number of tics and their intensity (the speed of tic-associated body movements; see Star Methods). Chemogenetic inhibition of bilateral ICs significantly reduced both tic frequency and intensity (Figures 5F and 5G; Video S3).

We next investigated whether the dmTh-IC pathway-specific chemogenetic inhibition affected tic generation. To test this issue, AAV2retro-CAGGS-Cre was injected into bilateral ICs and AAV DJ-EF1α-DIO-hM4Di-mCherry into bilateral dmTh (Figure 5B and 5D). Bilateral inhibition of this pathway significantly reduced tic intensity, while tic frequency was unchanged (Figures 5H and 5I; Video S3).

Because we used a relatively high dose of CNO (10 mg/kg) and CNO has been reported to influence glutamatergic and dopaminergic systems,[35,36] we conducted control experiments using mCherry-expressing viruses instead of hM4Di-mCherry (Figures 5A and 5B). CNO administration in these controls had no significant effect (Figure 5J-5M).

Taken together, these results indicate that the thalamo-insular pathway contributes to tic generation.

Chemogenetic inhibition of the thalamo-insular pathway alters downstream tic-associated cortical activity

We next examined whether chemogenetic manipulation of the thalamo-insular pathway altered activity in downstream cortical regions. Fiber photometry Ca^{2+} recordings were performed in the ipsilateral M1 and bilateral IC of mice in which IC-projecting dmTh neurons expressed inhibitory DREADD, using the same experimental timeline as in the preceding

experiment (Figure 6A). CNO administration reduced tic intensity without affecting tic frequency, consistent with behavioral data (Figures 5H, 5I, and S4). During the CNO session, tic-associated Ca^{2+} transients persisted (Figures 6B and 6C), but their amplitudes were significantly reduced in the ipsilateral M1 and ipsilateral IC (Figures 6C and 6D). In contrast, the amplitude of Ca^{2+} transients in the contralateral IC remained unchanged.

To further assess whether chemogenetic manipulation of the IC or the dmTh-IC pathway modulates M1 activity at the single-cell level, we performed two-photon Ca^{2+} imaging of GCaMP6f-expressing ipsilateral M1 neurons (Figure S5A). IC inhibition reduced Ca^{2+} event amplitudes in both superficial and deep layers, whereas the dmTh-IC pathway inhibition selectively reduced amplitudes in the superficial layer. Event frequency in the superficial layer was unaffected by either manipulation, while IC inhibition increased frequency in the deep layer. For response probability, both manipulations decreased tic-associated responses in the superficial layer, whereas only the dmTh-IC pathway inhibition increased responses in the deep layer (Figures S5B-M).

These results indicate that inhibition of IC neurons or IC-projecting dmTh neurons modulates M1 activity in a layer-specific manner, contributing to tic suppression.

DISCUSSION

We found that a mouse tic model induced by striatal disinhibition exhibited brain activation across motor and limbic structures, including the insular cortex. We further provided anatomical evidence that basal ganglia outputs originating from the striatal motor domain are transmitted to the insula via the intralaminar thalamic nuclei, which are known targets of DBS in intractable TS.[33,34] Finally, we demonstrated that chemogenetic inhibition of the thalamo-

insular pathway suppressed tic symptoms, indicating a causal role for this motor-limbic circuit in tic generation. Collectively, these findings reveal an unexpected crosstalk between motor and limbic domains within the CBGTC network and suggest that aberrant activity in the thalamo-insular pathway contributes to the emergence of tics.

Animal model of tic disorders based on striatal disinhibition

Motor and vocal tics accompanied by premonitory urges are the hallmark symptoms of TS patients. These individuals frequently manifest comorbid psychiatric and behavioral disorders, including OCD, ADHD, autism spectrum disorder (ASD), anxiety, depression, and sleep disorders.[7,8] Although recent genome-wide association studies (GWAS) or whole-exome sequencing studies have suggested some candidate genes contributing to TS pathophysiology, critical genes have not yet been identified.[37-39] Moreover, knockout mouse models of these candidate genes generally do not exhibit motor tics, or if they do, the frequency is very low. Instead, some of these models display stereotyped behaviors such as excessive grooming or rearing, which are more reminiscent of OCD.[40,41] In contrast, postmortem studies in TS patients have revealed a reduction of striatal GABAergic interneurons.[21,22] Consistent with these findings, nonhuman primate models of motor and vocal tics induced by blocking GABAergic inputs have been well established (see also Figures 1 and S1 in our study).[15-19,42] Beyond striatal interneurons, the striatum is also known to receive substantial inputs from "arkypallidal" neurons in the GP (corresponding to the external globus pallidus [GPe] in primates; see also Figure S1A).[43] Indeed, injections of a $GABA_A$ receptor antagonist into the primate GPe induce choreic dyskinesias.[44-46] Thus, dysfunction of the striato-GP networks through disruption of GABAergic tone may generate rhythmic activity in BG output neurons and subsequently M1 neurons, ultimately leading to involuntary movements.[42,47,48]

The insula is a key site responsible for tic generation

Our study demonstrated that the IC is robustly activated in a mouse model of tics induced by striatal disinhibition (Figure 2). Tic-associated activity was observed not only in the IC but also in the M1 (Figures 3, 6, S2, and S5). Importantly, chemogenetic inhibition of the IC alleviated tic-like behaviors (Figure 4). These findings strongly suggest that the IC serves as a key site responsible for tic generation. Supporting this notion, human-imaging studies in TS patients have demonstrated IC activation.[27,28]

Intriguingly, we previously reported that the use of an oral splint, typically applied in the treatment of temporomandibular disorders, produced immediate and marked therapeutic effects on both motor and vocal tics in approximately two-thirds of TS patients.[49] Motivated by this clinical observation, we sought to anatomically identify the ascending pathway of orofacial proprioception in rodents, given that oral devices activate muscle spindles of the masseter. We identified that orofacial proprioceptive inputs are ultimately transmitted not to the primary sensory cortex, but to the IC via the supratrigeminal nucleus (Su5) and the caudo-ventromedial subdivision of ventral posteromedial thalamic nucleus (VPMcvm).[50,51] Taken together, these anatomical and clinical findings suggest that oral splint insertion may modulate aberrant IC activity underlying tic generation in TS patients.

The IC is well known as a center of emotional processing and interoception awareness, integrating signals generated by physiological body states.[52-54] In this context, abnormal IC activity in TS patients may contribute not only to motor symptoms such as tics but also to premonitory urges and comorbid psychiatric disorders, including OCD, ADHD, and ASD.

Why the intralaminar thalamic nuclei can be surgical targets in TS patients

Historically, ablative procedures such as thalamotomy and pallidotomy were pioneering neurosurgical treatments for patients with movement disorders.[55,56] Since the development of DBS at the end of the last century, DBS targeting the internal globus pallidus (GPi) or the STN has become the gold standard for patients with intractable Parkinson's disease and dystonia.[57,58] In contrast, the ITN have empirically been effective targets for DBS in TS patients.[59,60] However, the mechanistic basis for this efficacy has remained unclear.

Anatomically, our study identified the dmTh, particularly the rITN, as a candidate region relaying BG output to the IC (Figure 4). Chemogenetic inhibition of IC-projecting dmTh neurons attenuated tic-associated activity in the IC (Figure 5). Moreover, this manipulation also suppressed tic-related activity in the M1 and reduced the expression of tic-like movements (Figures 6, S4, and S5). These results suggest that the dmTh-IC pathway transmits abnormal BG activity to the IC, thereby contributing to the exacerbation of motor tics.

Importantly, caudal ITN (cITN; corresponding to the Pf in rodents), a clinical DBS target in TS patients, maintains topographically organized connections with the CBGTC circuits (particularly the striatum and cortex).[30,61] In contrast, the rITN exhibits widespread or loosely topographical projections to multiple structures within these circuits.[62] Given that the rITN and cITN are spatially adjacent, the current spread from a DBS electrode implanted in the cITN may also influence the rITN, thereby exerting therapeutic effects in TS patients. A future double-blinded clinical study comparing the efficacy of rITN versus cITN stimulation will be warranted to determine the optimal surgical target.

Crosstalk in motor and limbic networks in the cortico-basal ganglia-thalamo-cortical circuits

Crosstalk between motor and limbic networks within the CBGTC circuits has long been debated. These circuits are traditionally conceived as functionally segregated, closed parallel

loops, which include motor, associative, and limbic loops originating from distinct cortical regions.[63,64] Consistent with this view, pharmacological manipulations of the motor, associative, and limbic domains of the striatum or GPe selectively induce motor, cognitive, and emotional disturbances, respectively.[65]

However, our findings challenge this closed-loop model by demonstrating that, in addition to the previously described "limbic-to-motor" open loop,[32] there exists a complementary "motor-to-limbic" open loop (striato-SNr-dmTh-insula pathway). These data reveal bidirectional interactions between motor and limbic domains within the CBGTC circuits. This framework may explain a wide range of symptoms observed in TS patients, such as motor and vocal tics, premonitory urges, and psychiatric comorbidities including OCD and ADHD. Dysfunction in the "motor-to-limbic" pathway may allow abnormal motor signals to spread into limbic regions, leading to emotional and cognitive symptoms. Since the IC does not have strong projections to the M1,[66] aberrant IC activity likely influences motor outputs indirectly through other cortical structures such as the sensory cortex, or via subcortical feedback loops. In addition, tic-associated cortical activity in the M1 or IC may not necessarily precede tic onset, suggesting that abnormal communication within the CBGTC network is dynamic and recurrent.

In conclusion, our study suggests that normalization of IC activity could restore balance between motor and limbic circuits, and improve both motor and emotional symptoms in TS.

EXPERIMENTAL MODEL AND SUBJECT DETAILS

Animals

All animal procedures were approved by the Institutional Animal Care and Use Committees of Kobe University. Male C57BL/6J (aged 6−16 weeks) and male PV-Cre mice (aged 6–10 weeks) were used for experiments, which were maintained at the animal facility of Kobe University. Animals were group-housed under controlled temperature (23−25 ℃) in a 12/12 h light-dark cycle (light cycle from 6 AM to 6 PM) with free access to food and water. Animals implanted with a guide cannula or optical fibers were single-housed after the surgery to prevent damage to the equipment.

METHOD DETAILS

Head plate attachment

The first surgery was performed in mice aged 6−10 weeks. Mice were anesthetized with ketamine (80 mg/kg, intraperitoneally [i.p.]; Ketalar, Daiichi Sankyo, Tokyo, Japan) and xylazine (12 mg/kg, i.p.; Seractar, Elanco Japan, Tokyo, Japan), and mounted on a stereotaxic apparatus (SR-6M-HT, Narishige, Tokyo, Japan). Gentamicin eye ointment (TAKATA Pharmaceutical Co., Saitama, Japan) was used to prevent corneal drying. After subcutaneous injection of epinephrine-containing lidocaine (Xylocaine DENTAL, Dentsply Sirona, York, PA, USA), the scalp was removed to expose the skull. Except for anatomical neuronal tracing experiments, a custom-made metal head plate was affixed to the skull with dental cement (G-CEM ONE neo, GC.dental, Tokyo, Japan) to secure the mouse to a home-made fixation apparatus.

Viral injection

For viral delivery, a small craniotomy was typically performed on the same day as the head plate attachment. A small hole was made using a dental drill (MICROMOTOR LM-III, GC.dental), with supplementary ketamine/xylazine administered if necessary. Viral solutions were pressure-injected through a glass micropipette attached to a microinjector (I-31, Narishige, Tokyo, Japan). The micropipette was left in place for at least 5 min to allow viral diffusion. All stereotaxic coordinates were based on the Paxinos Mouse Brain Atlas (third version).[67]

For viral tracing experiments, AAV1-CAG-tdTomato (2.0×10^{13} vector genomes [vg]/ml, diluted 1:2 in saline) or AAV1-CAG-Flex-tdTomato (1.6×10^{13} vg/ml, diluted 1:2 in saline) was injected unilaterally into the dorsal striatum (dSTR; 0.10−0.15 µl/injection; AP: 0.0 mm, ML: 2.7 mm, DV: –3.5 mm) or the substantia nigra pars reticulata (SNr; 0.10−0.15 µl/injection; AP: –3.1 mm, ML: 1.65 mm, DV: –4.6 mm). AAV2retro-CAGGS-EGFP (6.8×10^{12} vg/ml, diluted 1:2 in saline) or a mixture of AAV2retro-CAGGS-EGFP and AAV1-CAG-tdTomato (diluted 1:1:1 in saline; red fluorescence data not shown) was injected into the rostrocaudally middle part of insular cortex (IC; 0.10−0.15 µl/injection; AP: 0.5 mm, ML: 3.3 mm, DV: –3.6 mm). For labeling dorsomedial thalamus (dmTh)-projecting neurons in other brain regions, AAV2retro-CAGGS-Cre (7.3×10^{12} vg/ml, diluted 1:2 in saline) was injected into the dmTh (0.20 µl/injection; AP –1.5 mm, ML: 0.5 mm, DV: –3.5 mm).

For experiments targeting IC neurons with hM4Di-mCherry or mCherry using the designer receptors exclusively activated by designer drugs (DREADD) system, AAV8-hSyn-hM4Di-mCherry (2.2×10^{13} vg/ml, diluted 1:2 in saline) or AAV8-hSyn-mCherry (2.1×10^{13} vg/ml, diluted 1:2 in saline) was injected bilaterally into rostrocaudally distinct IC sites: anterior IC (aIC; 0.20 µl/injection, AP: 1.5 mm, ML: ±2.7 mm, DV: –3.2 mm), middle IC (mIC; 0.30

μl/injection, AP: 0.5 mm, ML: ±3.3 mm, DV: –3.6 mm), and posterior IC (pIC; 0.20 μl/injection, AP: –0.5 mm, ML: ±3.7 mm, DV: –3.5 mm).

For experiments targeting IC-projecting dmTh neurons with hM4Di-mCherry or mCherry, AAV2retro-CAGGS-Cre (7.3×10^{12} vg/ml, diluted 1:2 in saline) was injected bilaterally into the ICs (aIC, mIC, pIC; same coordinates as above), and AAVDJ-EF1α-DIO-hM4Di-mCherry (1.5×10^{13} vg/ml, diluted 1:2 in saline) or AAVDJ-EF1α-DIO-mCherry (2.0×10^{13} vg/ml, diluted 1:2 in saline) was injected bilaterally into the dmTh (0.40 μl/injection; AP: –1.5 mm, ML: ±0.5 mm, DV: –3.5 mm).

For fiber photometry, AAV1-Syn-GCaMP6f-WPRE-SV40 (2.0×10^{13} vg/ml, diluted 1:2 in saline) was injected unilaterally into the primary motor cortex (M1; 0.20 μl/injection, AP: 0.5 mm, ML: 1.0 mm, DV: –1.3 mm) or bilaterally into the mIC (0.20 μl/injection, AP: 0.5 mm, ML: 3.3 mm, DV: –3.6 mm). One week later, optical fibers (ferrule outside diameter 1.25 mm, 400 μm core, NA 0.5; cat# R-FOC-BL400C-50NA, RWD Life Science, Guangdong, China) were implanted 200 μm above the injection sites (M1 or mICs) and fixed with dental resin (UNIFAST II, GC.dental) under isoflurane anesthesia (1.0%; Viatris, Pittsburgh, PA, USA).

For two-photon microscopic imaging, a circular craniotomy (2.5 mm in diameter) was made over the ipsilateral M1 (center, AP: 0.5 mm, ML: 1.0 mm) under isoflurane anesthesia, 1-2 days after the head plate attachment. After the craniotomy, AAV1-Syn-GCaMP6f-WPRE-SV40 (2.0×10^{13} vg/ml, diluted 1:2 in saline) was injected into two depths of the ipsilateral M1 (300 μm and 500 μm below the brain surface, 0.20 μl for each injection). The cortical surface was covered with a glass window composed of two coverslips (2 and 4.5 mm in diameter, respectively; Matsunami Glass, Osaka, Japan), with the aid of transparent adhesive (NOR-61, Norland Products, Jamesburg, NJ, USA). The edges of the glass window were sealed with dental cement (Fuji Lute, GC.dental) and adhesive resin cement (Super Bond, Sun Medical,

Shiga, Japan).

EEG and EMG electrode implantation

In the experiments shown in Figures 1 and S1, EEG and EMG electrodes were implanted under ketamine/xylazine anesthesia on the same day as the head plate attachment. In the experiment shown in Figure 4, EEG electrodes were implanted three weeks after viral injections under isoflurane anesthesia.

For EEG electrode implantation, small craniotomy holes were made above the ipsilateral M1 (AP: 0.5 mm, ML: 1.0 mm) and the contralateral visual cortex (AP: –3.5 mm, ML: 3.0 mm; reference electrode). Metal screws, serving as electrodes, were implanted into the holes and secured to the skull with dental cement (G-CEM ONE neo, GC.dental). Screws were connected to custom-made terminal connectors via stainless-steel wires, and the connectors were mounted on the head plate using dental resin (UNIFAST II, GC.dental).

For EMG electrode implantation, mice received a subcutaneous injection of epinephrine-containing lidocaine in the contralateral upper arm. The skin was incised to expose the triceps, and two PFA-coated stainless-steel wires (7-strand, 0.0055” in diameter; cat# 793200, A-M Systems, Sequim, WA, USA) were inserted into the muscle and secured with tissue adhesive (Vetbond, 3M Co., Ltd, St. Paul, MN, USA) and suture thread. The implanted wires were connected to custom-made terminal connectors as described above.

Guide cannula implantation

When repeated bicuculline injections were required for DREADD experiments (see below for details), a guide cannula was chronically implanted into the unilateral dSTR to minimize variability in behavioral results due to differences in bicuculline injection sites. After

craniotomy under isoflurane anesthesia, a 5-mm-long guide cannula (AG-5T, Eicom, Kyoto, Japan) was implanted vertically into the dSTR (AP: 0.0 mm, ML: 2.7 mm, DV: –3.5 mm) for DREADD experiments without neuronal recording. For DREADD experiments combined with fiber photometry or two-photon calcium imaging, an 8-mm-long guide cannula (CXG-8T, Eicom) was implanted sagittally from caudal to rostral with a 40° angle to avoid interference with the optical fibers or cranial window. The guide cannula was then anchored to the skull with the dental cement (G-CEM ONE neo, GC.dental).

Striatal local bicuculline injection

Bicuculline methochloride (cat# B7686, Sigma, St. Louis, MO, USA) was dissolved in saline at 100 mg/ml to prepare stock aliquots, which were stored at −30℃. Immediately before each injection, the stock solution was diluted with saline to a final concentration of 0.2 mg/ml.

For single-injection experiments, a small craniotomy hole was made under isoflurane anesthesia, which was disconnected immediately afterward. A disposable glass micropipette filled with bicuculline was gently inserted into the dSTR (AP: 0.0 mm, ML: 2.7 mm, DV: –3.5 mm). After recording baseline behavioral data, bicuculline was injected using a glass micropipette attached to a microinjector (I-31, Narishige). The micropipette was kept in place until the end of the experiment to minimize tissue damage and prevent leakage into adjacent brain regions.

For repeated-injection experiments (e.g., in DREADD experiments), an injection cannula (AMI-5T or CXMI-8T, Eicom) attached to a microsyringe (cat# N1701; Hamilton, Reno, NV, USA) containing bicuculline solution was inserted into the chronically implanted guide cannula (see above).

In both injection protocols, 0.20 μl of bicuculline was injected over ~1 min.

Chemogenetic manipulation

To chemogenetically suppress the activity of specific neurons, the DREADD agonist, clozapine-N-oxide (CNO; cat# HY-17366, MedChemExpress, Monmouth Junction, NJ, USA), was administered intraperitonially in mice expressing hM4Di-mCherry or mCherry (control) in IC neurons or IC-projecting dmTh neurons. CNO was dissolved in dimethyl sulfoxide (DMSO; cat# 13445-74, Nacalai Tesque, Kyoto, Japan) at 100 mg/ml to prepare stock aliquots, which were stored at −30°C. The stock solution was diluted with saline to a final concentration of 2 mg/ml immediately before the experiments.

In the experiments shown in Figures 4, 5, S5, and S6, CNO or vehicle (2% DMSO) was administered at a dose of 5 ml/kg (i.p.; equivalent to 10 mg/kg CNO) 30 min before baseline recordings. Each trial was conducted at intervals of at least 72 h to avoid residual effects of CNO or bicuculline from the previous session.

EEG and EMG recordings

After the mice were secured in the head-fixation apparatus, EEG and EMG electrodes were connected to an amplifier with an integrated A/D converter (PowerLab 26T, ADInstruments, Dunedin, New Zealand). EEG and EMG signals were sampled at 10 kHz. Behavioral videos were simultaneously recorded at 100 Hz using a digital camera (acA800-510um, Basler, Ahrensburg, Germany) positioned in front of the mice.

Baseline recordings were obtained for 5 min before bicuculline injection. Following bicuculline injection, recordings continued for 40 min. The acquired EEG and EMG data were preprocessed in MATLAB (MathWorks, Natick, MA, USA). After downsampling to 1 kHz, the data were bandpass filtered (EEG: 0.5 – 120 Hz; EMG: 5 – 500 Hz) and subjected to 60-Hz

hum noise removal.

Fiber photometry recording

The implanted optical fibers in the ipsilateral M1 or bilateral ICs of mice expressing GCaMP6f in these brain regions were connected to a multichannel fiber photometry system (R821; RWD Life Science) via a bundle branching patch cord (BBP(4) 400/430/1100-0.57_2m_FCM-4xZF1.25(F)_LAF, Doric Lenses, Québec, Canada), which enabled simultaneous recording from multiple brain regions. Dual-wavelength recording (470 nm and 410 nm) was carried out, in which the 470-nm laser was used to detect GCaMP6f fluorescence signals and the 410-nm laser was used to measure calcium-independent isosbestic control signals. Neuronal Ca^{2+} signals and behavioral videos were recorded synchronously at 60 Hz. Recordings were conducted for 5 min before and 40 min after bicuculline injection.

Data were analyzed using custom-written MATLAB scripts. Briefly, both 470-nm and 410-nm signals were individually smoothed using a local linear regression filter to reduce high-frequency noise. The fitted control signal was obtained by regressing the 410-nm signal against the 470-nm signal using a quantile regression method. $\Delta F/F$ was calculated as (F-F1)/ F1, where F represents the 470-nm signal and F1 represents the fitted control signal.

***In vivo* two-photon microscopic calcium imaging**

Two-photon images were acquired from the mice expressing GCaMP6f in the ipsilateral M1 using an A1MP^{+} system (NIS-Elements, Nikon Instech Co., Ltd, Tokyo, Japan) equipped with a water-immersion ×10 objective lens (numerical aperture [NA], 0.3; working distance 3.5 mm; cat# MRH07120, Nikon Instech Co., Ltd) and a mode-locked Ti:sapphire Chameleon Ultra II laser (Chameleon Vision, Coherent, Santa Clara, CA, USA) set at 950 nm. To quantify

neuronal activity, time-sequential images were captured at a resolution of 512 × 512 pixels (scanning rate, 2 Hz; 2× digital zoom).

Before bicuculline injection, continuous 1000-frame images were obtained twice from the ipsilateral M1 at depths of 250 and 500 μm, respectively. After bicuculline injection, continuous 1000-frame images were captured again from the same fields of view. Images were repeatedly acquired for 5-25 min after bicuculline injection. As shown in Figures 1 and S1, this period corresponds to the time window in which tic-like movements were clearly observed.

Histology

Mice were deeply anesthetized with ketamine/xylazine and transcardially perfused with 4% paraformaldehyde (PFA). The brain was extracted, post-fixed in 4% PFA overnight, and soaked in 15% and then 30% sucrose for 2-3 days for dehydration. The brains were sectioned into 50-μm coronal slices on a microtome (OFT5000, Bright Instruments, Cambridgeshire, UK).

For c-Fos immunohistochemistry, brain slices were permeabilized with 0.5% Triton X-100 (Cat# 35501-15, Nacalai Tesque) in PBS for 3 h at room temperature. After blocking with 5% bovine serum albumin (BSA; Cat# 01860-36, Nacalai Tesque) for 1 h, the slices were incubated overnight at 4℃ with primary antibody against c-Fos (cat# sc-52, Santa Cruz Biotechnology, Dallas, TX, USA; 1:1000) diluted in PBS. After washing in PBS, the slices were incubated overnight at 4℃ with Cy3-conjugated anti-rabbit secondary antibody (cat# 711-165-152, Jackson ImmunoResearch, West Grove, PA; 1:1000) in PBS. The slices were then mounted on glass slides with DAPI-containing mounting medium (H-1200, Vector Laboratories, Newark, CA, USA).

Fluorescence images were captured using a KEYENCE BZ-X810 microscope

(KEYENCE, Osaka, Japan) or an Olympus FV-3000 confocal microscope (Olympus, Tokyo, Japan) equipped with a ×40 objective lens (NA 0.95; Olympus).

QUANTIFICATION AND STATISTICAL ANALYSIS

Behavioral analysis

Tic-like movements were quantified in head-fixed mice following unilateral striatal bicuculline injection. User-defined body parts were tracked using DeepLabCut (https://github.com/DeepLabCut).[68] A custom-made MATLAB script was used to compute the speed (i.e., velocity without directional components) and acceleration of movements in the contralateral wrist or the contralateral corner of the mouth based on the DeepLabCut tracking trajectories. Motor tics were detected based on the timing of spike signals in the ipsilateral M1 cortical activity obtained from EEG or fiber photometry recordings (see below for details), as the M1 spikes consistently preceded motor tics (Figures 1, 3, and S1). For EEG-based tic detection, the speed of body movements was calculated in a 0–0.3 s time window after M1 spikes. For fiber photometry-based tic detection, the speed was calculated in a −0.2–+0.1 s window relative to the M1 spike, as tic-related Ca^{2+} transients typically lagged behind the onset of tic-like movements by ~0.2 s (see Figure 3).

In Figures 1 and S1, the area under the curve (AUC) of movement speed of the contralateral wrist and mouth was calculated in a 0–0.3 s time window after EEG spikes associated with tics as follows:

$$\text{AUC} = \sum_{t=1}^{0.3\times Fs} St \times \frac{1}{Fs}$$

, where *St* is the speed of the targeted body part at each time point after an EEG spike, and Fs is the sampling frequency of the behavioral video (typically 100 Hz).

A movement was classified as a motor tic if the speed of the contralateral wrist or corner of the mouth exceeded the mean + 0.5 SD and the maximum acceleration exceeded the mean + 2 SD of the entire recording period. This automated detection method was largely consistent with tic identification by visual inspection. Tic intensity was calculated as $(S_{wrist}/S1_{wrist} + S_{mouth}/S1_{mouth})/2$, where S is the average speed of the contralateral wrist or contralateral corner of the mouth during tic expression (0-30 after bicuculline injection) and S1 is that of the first test (vehicle injection). The relative intensity value of the first test was therefore set to 1.

During *in vivo* two-photon imaging, we monitored mouse behavior with an analog infrared-sensitive CCD camera. Due to the low light intensity, image resolution was insufficient for accurate tracking of mouth-corner movements. Therefore, only forelimb trajectories were used to assess tic-like movements. Forelimb tics were automatically detected when their speed exceeded the mean + 0.5 SD and their peak acceleration exceeded the mean + 2 SD. Although this method relied solely on forelimb speed, the detected onset times of tic-like movements were largely consistent with those identified by a well-trained observer.

Image analysis

Images were analyzed using Fiji/ImageJ (National Institutes of Health, Bethesda, MD, USA) and MATLAB.

For counting c-Fos positive cells in Figure 2, images were binarized using the built-in auto-threshold “Triangle” function in ImageJ. After the background noise was removed using the “Remove Outliers” function, c-Fos positive cells were automatically counted with the “Analyze Particles” function.

For counting virally EGFP-labeled thalamic neurons in Figures 4 and S3, coronal sections containing target brain regions were selected at 300-µm intervals, and EGFP-positive cells were manually counted. Cell counts from all sections in each thalamic region were summed and normalized to the value of the ventromedial (VM) thalamus.

For quantifying the density of axonal terminals originating from the substantia nigra pars reticulata (SNr), the following value was calculated:

$$F = (F_{Mean} - F_{1\%})/F_{background}$$

, where F_{Mean} is the mean fluorescence intensity within the target region, $F_{1\%}$ is the 1st percentile of fluorescence intensity within the same region (used to correct for autofluorescence), and $F_{background}$ is the mean background fluorescence intensity (used to normalize across imaging sessions). The resulting values were then normalized to those of the VM thalamus.

Two-photon Ca^{2+} images were corrected for focal plane displacement using the "TurboReg" plug-in in ImageJ. To estimate neuronal activity, regions of interest (ROIs) were determined using a semi-automated MATLAB-based toolbox with a graphical user interface (EZcalcium; https://github.com/porteralab/EZcalcium).[69] To evaluate synchronized neuronal activity in M1, Pearson's correlation coefficient was calculated using Ca^{2+} transient values from each ROI. A Ca^{2+} event was defined as a signal elevation with a peak amplitude exceeding the baseline + 2 SD, where the baseline was defined as the 35th percentile of the total fluorescence distribution.[70] The mean amplitude and frequency of Ca^{2+} events were calculated for each detected neuron.

To assess response probability, we quantified how reliably each neuron responded to tic-like movements. A neuron was considered "responsive" if the fluorescence intensity during the two frames following tic onset increased by more than 2 SD compared with the

two frames preceding the onset. Response probability was calculated by dividing the number of responsive events by the total number of tic events.

For Figure S2H, shuffled tic onset data were generated using the "randperm" function in MATLAB. The shuffling and response probability calculation were repeated 100 times, and the median value was used for statistical analysis (see below).

Spike detection

In the analyses of EEG and fiber photometry data, preprocessed signals (as described in the sections of "EEG and EMG recordings" and "Fiber photometry recording") were converted into robust z score, and peaks with a prominence of at least 1 × normalized interquartile range (NIQR) were detected using the "findpeaks" function in MATLAB. The prominence values of the detected peaks were then subjected to k-means clustering to determine the detection threshold automatically. For EEG data, the number of clusters was set to 3; for fiber photometry data, it was set to 4. Peaks classified into the cluster with the lowest prominence were excluded as non-spike events, and the remaining peaks were defined as spike signals. The robust z score was calculated as:

$$\text{Robust z score} = (x - \text{median}[x])/\text{NIQR}$$

, where NIQR was obtained by converting the interquartile range (IQR, representing the central 50% of the distribution) to the equivalent of 1 SD in a normal distribution by multiplying by a normalization factor of 0.7413.

Statistics

Statistical analyses were performed using MATLAB and R (version 4.4.2; with the "tidyverse", "rstatix", "afex", "emmeans" packages). Details of statistical tests are provided in

the figure legends. Statistical tests included paired or unpaired Welch's *t*-test, one-sample *t*-tests with Holm correction, one-way analysis of variance (ANOVA) with independent or repeated-measures, followed by pairwise *t*-tests with Holm correction, Wilcoxon signed-rank test, and Kruskal-Wallis test, followed by Dunn's multiple comparison tests with Holm correction.

We did not routinely perform formal tests for normality, as their results are highly sensitive to sample size. When the sample size was large ($n > 30$), t-tests were generally robust to moderate deviations from normality. In such cases, we visually inspected the data distribution and applied parametric tests unless the data exhibited extreme skewness or kurtosis. When the sample size was small, we considered it difficult to reliably estimate the population distribution and generally used parametric tests unless there was a clear reason to assume non-normality.

Data analyzed with parametric tests are presented as mean ± SEM, while those analyzed with non-parametric tests are shown as box plots. Box plots indicate the 25th and 75th percentiles, the median, and whiskers extending to data within a 1.5 x IQR. All tests were two-tailed with significance set at $\alpha = 0.05$.

ACKNOWLEDGMENTS

We thank A. Nambu, K. Toda, T. Hirata, K. Tamada, N. Nakai, and Y. Shintani for their valuable comments and discussion. We are grateful to H. Shima and M. Shiramizu for their assistance with animal care. This work was supported by the Japan Society for the Promotion of Science (JSPS) KAKENHI (18K06852, 22K19732 and 24H00422, and 24K02339) and by the Taiju Life Social Welfare Foundation to Y.T.

AUTHOR CONTRIBUTIONS

H.K. and Y.T. conceived the study and designed the experiments. H.K. performed the majority of the experiments, and N.T. conducted some of the histological experiments. H.K. analyzed the data. K.K. provided materials. H.K. and Y.T. wrote the manuscript with editorial input from T.T.

DECLARATION OF INTERESTS

The authors declare no competing interests.

FIGURE LEGEND

Figure 1. Striatal disinhibition induces tic-like movements and tic-related EEG spikes in the ipsilateral primary motor cortex (M1).

(A) Schematic of electrophysiological recordings in the unilateral striatal bicuculline-induced tic mouse model.

(B) Coronal brain section showing the injection site in the dorsal striatum (dSTR; arrow). Scale bar, 500 μm.

(C and D) Representative traces of electroencephalogram (EEG) from the ipsilateral primary motor cortex (M1; gray), electromyogram (EMG) from the contralateral triceps muscle (red), and wrist movement speed of the contralateral forelimb (blue) following bicuculline injection. Black arrows indicate tic-like movement onsets. The region outlined by the red dashed rectangle in (C) is shown at higher magnification in (D).

(E) Averaged traces of EMG from the contralateral triceps muscle (pink) and wrist movement speed (blue), aligned to the onsets of EEG spikes recorded in the ipsilateral M1 during the 40-min period following bicuculline injection (n = 9 mice). The black arrow indicates the mean latency of tic onsets relative to EEG spike onsets. The shaded area represents ± SEM.

(F-H) Time course of tic counts (F) and the frequency (G) and mean amplitude (H) of EEG spikes recorded in the ipsilateral M1, plotted in 5-min bins after bicuculline injection (n = 9 mice).

(I) Averaged traces of EMG from the contralateral triceps muscle (pink) and wrist movement speed (blue), aligned to the onsets of EEG spikes recorded in the ipsilateral M1, shown for successive 10-min epochs following bicuculline injection (n = 9 mice). Data are presented in the same format as in (E).

(J and K) Time course of mean EMG amplitude (J) and the area under the curve (AUC) of the contralateral wrist movement speed (K) within the 0.3-s window following tic-like movement onsets, plotted in 10-min bins after bicuculline injection (n = 9 mice).

(L) Representative traces showing EEG spikes in the ipsilateral M1 not accompanied by tic-like movements (black arrows).

(M) Time course of the percentage of EEG spikes accompanied by tic-like movements, plotted in 10-min bins after bicuculline injection (n = 9 mice). For (H) and (M), if no EEG spikes occurred in a given time bin, the value for that bin was set to 0 for individual data points;

however, these bins were excluded from group means and SEM.

Data are presented as mean ± SEM; individual mouse data are shown in gray.

See also Figures S1 and S2 and Video S1.

Figure 2. Tic-associated brain activation revealed by c-Fos immunohistochemistry

(A) Experimental timeline. Ninety minutes after unilateral bicuculline injection into the dSTR, mice were perfused, paraformaldehyde-fixed, and brain sections were processed for c-Fos immunohistochemistry. Top right, representative coronal section showing the striatal injection site (arrow) stained for c-Fos. Scale bar, 500 µm.

(B) Representative images of c-Fos immunostaining in the contralateral and ipsilateral dSTR at the anteroposterior (AP) level of +0.26 mm from the bregma. Scale bar, 500 µm.

(C) Representative c-Fos immunostaining in selected brain regions across cortical, basal ganglia, thalamic, and limbic structures. Scale bars, 500 µm.

(D) Quantification of c-Fos-positive cells in the contralateral (gray) and ipsilateral (pink) hemispheres across brain regions. Data are presented as mean ± SEM; individual mouse data are shown in gray (n = 8 mice). Statistical analyses were performed using paired *t*-tests (*p*-values were not corrected for multiple comparisons). *$p < 0.05$; **$p < 0.01$; ***$p < 0.001$.

Abbreviations: Amyg, amygdala; Cg1, cingulate cortex area 1; cITN, caudal intralaminar thalamic nuclei; CL, centrolateral thalamic nucleus; CM, central medial thalamic nucleus; DP, dorsal peduncular cortex; GP, globus pallidus; IC, insular cortex; IL, infralimbic cortex; IMD, intermediodorsal thalamic nucleus; M2, secondary motor cortex; MD, mediodorsal thalamic nucleus; PC, paracentral thalamic nucleus; Pf, parafascicular thalamic nucleus; Pir, piriform cortex; Po, posterior thalamic nuclear group; PrL, prelimbic cortex; PV, paraventricular thalamic nucleus; rITN, rostral intralaminar thalamic nuclei; STN, subthalamic nucleus; VA,

ventral anterior thalamic nucleus; VL, ventrolateral thalamic nucleus; VM, ventromedial thalamic nucleus; VPL, ventral posterolateral thalamic nucleus; VPM, ventral posteromedial thalamic nucleus.

Figure 3. Insular cortical activity is associated with tic generation

(A) Schematic of fiber photometry recordings (top). AAV1-Syn-GCaMP6f was injected into the ipsilateral M1 and bilateral IC. Representative coronal sections showing GCaMP6f-expressing regions and optic fiber placements (dashed lines) in the M1 and IC (bottom). Scale bars, 500 μm.

(B) Representative traces of Ca^{2+} signals in the ipsilateral M1, ipsilateral IC, and contralateral IC following unilateral bicuculline injection. Wrist and mouth corner movement speeds are also shown.

(C) Averaged Ca^{2+} signals in the ipsilateral M1, ipsilateral IC, and contralateral IC, aligned to tic onsets during the 40-min post-injection period (n = 8 mice).

(D) Same data as in (C), shown for successive 10-min epochs. Shaded areas represent ± SEM.

(E) Time course of mean amplitudes of tic-related Ca^{2+} signals in the ipsilateral M1, ipsilateral IC, and contralateral IC, plotted in 10-min bins after bicuculline injection. Data are presented as mean ± SEM.

Figure 4. The intralaminar thalamic nuclei relay basal ganglia output to the insular cortex

(A) Anterograde tracing from the dSTR. Injection of AAV1-CAG-tdTomato into the dSTR labeled axon terminals in the GP, entopeduncular nucleus (EP), and substantia nigra pars reticulata (SNr), but not in the M1, M2, or IC. Representative coronal sections at the indicated AP levels are shown. Scale bar, 500 μm.

(B) Retrograde tracing from the IC. Injection of AAV2retro-CAGGS-EGFP into the rostrocaudally middle IC labeled neurons in the dorsomedial thalamus (dmTh), including the rITN, PV/intermediodorsal thalamic nuclei (IMD), and MD, but not in the striatum or other basal ganglia nuclei (GP, EP, STN, and SNr). Minimal labeling was observed in the motor thalamus (VM, and VA/VL) and Pf. tdTomato fluorescence in the IC is shown for reference as the injection site. Scale bars, 500 μm.

(C) Quantification of thalamic inputs to the IC, expressed as the $\log_{10}$ ratio of labeled neurons relative to the number of neurons in the VM thalamus (n = 5 mice). Data are presented as mean (black dots) ± SEM.

(D) Anterograde tracing from parvalbumin (PV)-positive neurons in the SNr of PV-Cre mice. Injection of AAV1-FLEX-tdTomato revealed widespread projections to multiple thalamic regions, including the dmTh. Scale bars, 500 μm.

(E) Triple viral tracing strategy to assess connectivity between the SNr and IC via the dmTh. AAV2retro-CAGGS-Cre was injected into the dmTh, AAV1-FLEX-tdTomato into the SNr, and AAV2retro-CAGGS-EGFP into the IC. Axon terminals from the SNr (tdTomato, red) were apposed to the somata of IC-projecting dmTh neurons (EGFP, green), particularly within the rITN. White rectangles in the thalamic regions in the top-right panels (scale bars, 500 μm) indicate areas shown at higher magnification in the bottom-right panels (scale bars, 50 μm), highlighting the appositions.

Abbreviations: Cla, claustrum; cp, cerebral peduncle; En, endopiriform nucleus; HPC, hippocampus; ic, internal capsule; LD, laterodorsal thalamic nucleus; mPFC, medial prefrontal cortex; Rh, rhomboid thalamic nucleus; S2, secondary somatosensory cortex; VP, ventral pallidum; ZI, zona incerta.

See also Figure S3.

Figure 5. Chemogenetic inhibition of the thalamo-insular pathway alleviates tic-like movements

(A and B) Schematic of the experimental setup for chemogenetic inhibition of the insular cortex (IC) or the thalamo-insular pathway. To inhibit the IC, AAV8-hSyn-hM4Di-mCherry (or control AAV8-hSyn-mCherry) was bilaterally injected into three rostrocaudally distinct sites of the IC. To specifically inhibit the thalamo-insular pathway, AAV2retro-CAGGS-Cre was bilaterally injected into the IC and AAV-DJ-EF1α-DIO-hM4Di-mCherry (or control AAV-DJ-EF1α-DIO-mCherry) into the bilateral dmTh.

(C and D) Representative coronal sections showing hM4Di-mCherry-expressing regions in the IC (C) or the dmTh and IC (D). AP coordinates from the bregma are indicated. Scale bars, 500 μm.

(E) Experimental timeline. Mice received repeated unilateral bicuculline injections into the dSTR via a chronically implanted guide cannula following intraperitoneal administration of vehicle (1st test), clozapine-N-oxide (CNO, 10 mg/kg; 2nd test), and vehicle (3rd test).

(F and G) Chemogenetic inhibition of the bilateral ICs reduced both tic frequency (F) and tic intensity (G) during the 30-min period following bicuculline injection (n = 8 mice).

(H and I) Chemogenetic inhibition of the bilateral dmTh-IC pathways reduced tic intensity (I), but not tic frequency (H) (n = 8 mice).

(J-M) Control experiment using mCherry-expressing viruses in the bilateral ICs (J, K) or the bilateral dmTh-IC pathways (L, M) showed no effects of CNO administration. (n = 8 mice for each group).

(F-M), Data are presented as mean ± SEM; individual mouse data are shown as gray circles. Statistical analyses were performed using one-way repeated measures ANOVA

followed by pairwise *t*-tests with Holm correction (F, H, J, and L) or one-sample *t*-tests with Holm correction (G, I, K, and M). ns, not significant; **p < 0.01; ***p < 0.001.

See also Video S3.

Figure 6. Chemogenetic inhibition of the thalamo-insular pathway alters downstream tic-associated cortical activity

(A) Schematic of the experimental setup for fiber photometry recording during chemogenetic inhibition of the thalamo-insular pathway. To inhibit the thalamo-insular pathway, AAV2retro-CAGGS-Cre was bilaterally injected into the IC, and AAV-DJ-EF1α-DIO-hM4Di-mCherry (or control AAV-DJ-EF1α-DIO-mCherry) into the bilateral dmTh. AAV1-Syn-GCaMP6f was injected into the ipsilateral M1 and bilateral IC for fiber photometry recordings. Following implantation of a guide cannula and optical fibers, tic-like movements were induced by repeated unilateral bicuculline injections into the dSTR under vehicle (1st test), CNO (10 mg/kg; 2nd test), and vehicle (3rd test) conditions.

(B) Representative traces of Ca^{2+} signals in the ipsilateral M1, ipsilateral IC, and contralateral IC following unilateral bicuculline injection during vehicle (left) and CNO (right) sessions. Wrist and mouth corner movement speeds are also shown.

(C) Average tic-aligned Ca^{2+} signals in the ipsilateral M1, ipsilateral IC, and contralateral IC, across three sessions (n = 8 mice). The shaded area represents ± SEM.

(D) Quantification of tic-related Ca^{2+} amplitudes in the ipsilateral M1, ipsilateral IC, and the contralateral IC (n = 8 mice). Chemogenetic inhibition of the dmTh-IC pathway significantly reduced Ca^{2+} amplitudes in the ipsilateral M1 and ipsilateral IC, but not in the contralateral IC. Data are presented as mean ± SEM; individual mouse data are shown as gray circles. Statistical analyses were performed using one-way repeated measures ANOVA followed by pairwise *t*-

tests with Holm correction. ns, not significant; *$p < 0.05$.

See also Figures S5 and S6.

REFERENCES

1. *Diagnostic and statistical manual of mental disorders : DSM-5-TR*. (2022). (American Psychiatric Association Publishing). 10.1176/appi.books.9780890425787.
2. Bullen, J.G., and Hemsley, D.R. (1983). Sensory experience as a trigger in Gilles de la Tourette's syndrome. J Behav Ther Exp Psychiatry *14*, 197-201. 10.1016/0005-7916(83)90048-4.
3. Kurlan, R., Lichter, D., and Hewitt, D. (1989). Sensory tics in Tourette's syndrome. Neurology *39*, 731-734. 10.1212/wnl.39.5.731.
4. Leckman, J.F., Walker, D.E., and Cohen, D.J. (1993). Premonitory urges in Tourette's syndrome. Am J Psychiatry *150*, 98-102. 10.1176/ajp.150.1.98.
5. Houghton, D.C., Capriotti, M.R., Conelea, C.A., and Woods, D.W. (2014). Sensory Phenomena in Tourette Syndrome: Their Role in Symptom Formation and Treatment. Curr Dev Disord Rep *1*, 245-251. 10.1007/s40474-014-0026-2.
6. Jankovic, J. (2001). Tourette's syndrome. N Engl J Med *345*, 1184-1192. 10.1056/NEJMra010032.
7. Leckman, J.F. (2002). Tourette's syndrome. Lancet *360*, 1577-1586. 10.1016/S0140-6736(02)11526-1.
8. Johnson, K.A., Worbe, Y., Foote, K.D., Butson, C.R., Gunduz, A., and Okun, M.S. (2023). Tourette syndrome: clinical features, pathophysiology, and treatment. Lancet Neurol *22*, 147-158. 10.1016/S1474-4422(22)00303-9.
9. Robertson, M.M. (2008). The prevalence and epidemiology of Gilles de la Tourette syndrome. Part 1: the epidemiological and prevalence studies. J Psychosom Res *65*, 461-472. 10.1016/j.jpsychores.2008.03.006.
10. Knight, T., Steeves, T., Day, L., Lowerison, M., Jette, N., and Pringsheim, T. (2012). Prevalence of tic disorders: a systematic review and meta-analysis. Pediatr Neurol *47*, 77-90. 10.1016/j.pediatrneurol.2012.05.002.
11. Scharf, J.M., Miller, L.L., Gauvin, C.A., Alabiso, J., Mathews, C.A., and Ben-Shlomo, Y. (2015). Population prevalence of Tourette syndrome: a systematic review and meta-analysis. Mov Disord *30*, 221-228. 10.1002/mds.26089.
12. Jafari, F., Abbasi, P., Rahmati, M., Hodhodi, T., and Kazeminia, M. (2022). Systematic Review and Meta-Analysis of Tourette Syndrome Prevalence; 1986 to 2022. Pediatr Neurol *137*, 6-16. 10.1016/j.pediatrneurol.2022.08.010.
13. Seideman, M.F., and Seideman, T.A. (2020). A Review of the Current Treatment of Tourette Syndrome. J Pediatr Pharmacol Ther *25*, 401-412. 10.5863/1551-6776-25.5.401.
14. Yael, D., Israelashvili, M., and Bar-Gad, I. (2016). Animal Models of Tourette Syndrome-From Proliferation to Standardization. Front Neurosci *10*, 132. 10.3389/fnins.2016.00132.

15. Tarsy, D., Pycock, C.J., Meldrum, B.S., and Marsden, C.D. (1978). Focal contralateral myoclonus produced by inhibition of GABA action in the caudate nucleus of rats. Brain *101*, 143-162. 10.1093/brain/101.1.143.
16. Bronfeld, M., Yael, D., Belelovsky, K., and Bar-Gad, I. (2013). Motor tics evoked by striatal disinhibition in the rat. Front Syst Neurosci *7*, 50. 10.3389/fnsys.2013.00050.
17. Crossman, A.R., Mitchell, I.J., Sambrook, M.A., and Jackson, A. (1988). Chorea and myoclonus in the monkey induced by gamma-aminobutyric acid antagonism in the lentiform complex. The site of drug action and a hypothesis for the neural mechanisms of chorea. Brain *111 (Pt 5)*, 1211-1233. 10.1093/brain/111.5.1211.
18. McCairn, K.W., Bronfeld, M., Belelovsky, K., and Bar-Gad, I. (2009). The neurophysiological correlates of motor tics following focal striatal disinhibition. Brain *132*, 2125-2138. 10.1093/brain/awp142.
19. Worbe, Y., Baup, N., Grabli, D., Chaigneau, M., Mounayar, S., McCairn, K., Féger, J., and Tremblay, L. (2009). Behavioral and movement disorders induced by local inhibitory dysfunction in primate striatum. Cereb Cortex *19*, 1844-1856. 10.1093/cercor/bhn214.
20. Kawaguchi, Y., Wilson, C.J., Augood, S.J., and Emson, P.C. (1995). Striatal interneurones: chemical, physiological and morphological characterization. Trends Neurosci *18*, 527-535. 10.1016/0166-2236(95)98374-8.
21. Kalanithi, P.S., Zheng, W., Kataoka, Y., DiFiglia, M., Grantz, H., Saper, C.B., Schwartz, M.L., Leckman, J.F., and Vaccarino, F.M. (2005). Altered parvalbumin-positive neuron distribution in basal ganglia of individuals with Tourette syndrome. Proc Natl Acad Sci U S A *102*, 13307-13312. 10.1073/pnas.0502624102.
22. Kataoka, Y., Kalanithi, P.S., Grantz, H., Schwartz, M.L., Saper, C., Leckman, J.F., and Vaccarino, F.M. (2010). Decreased number of parvalbumin and cholinergic interneurons in the striatum of individuals with Tourette syndrome. J Comp Neurol *518*, 277-291. 10.1002/cne.22206.
23. Shapiro, E., Shapiro, A.K., Fulop, G., Hubbard, M., Mandeli, J., Nordlie, J., and Phillips, R.A. (1989). Controlled study of haloperidol, pimozide and placebo for the treatment of Gilles de la Tourette's syndrome. Arch Gen Psychiatry *46*, 722-730. 10.1001/archpsyc.1989.01810080052006.
24. Kelley, A.E., Lang, C.G., and Gauthier, A.M. (1988). Induction of oral stereotypy following amphetamine microinjection into a discrete subregion of the striatum. Psychopharmacology (Berl) *95*, 556-559. 10.1007/BF00172976.
25. Conceição, V.A., Dias, Â., Farinha, A.C., and Maia, T.V. (2017). Premonitory urges and tics in Tourette syndrome: computational mechanisms and neural correlates. Curr Opin Neurobiol *46*, 187-199. 10.1016/j.conb.2017.08.009.
26. Jackson, S.R., Loayza, J., Crighton, M., Sigurdsson, H.P., Dyke, K., and Jackson, G.M. (2020).

The role of the insula in the generation of motor tics and the experience of the premonitory urge-to-tic in Tourette syndrome. Cortex *126*, 119-133. 10.1016/j.cortex.2019.12.021.

27. Bohlhalter, S., Goldfine, A., Matteson, S., Garraux, G., Hanakawa, T., Kansaku, K., Wurzman, R., and Hallett, M. (2006). Neural correlates of tic generation in Tourette syndrome: an event-related functional MRI study. Brain *129*, 2029-2037. 10.1093/brain/awl050.
28. Lerner, A., Bagic, A., Boudreau, E.A., Hanakawa, T., Pagan, F., Mari, Z., Bara-Jimenez, W., Aksu, M., Garraux, G., Simmons, J.M., et al. (2007). Neuroimaging of neuronal circuits involved in tic generation in patients with Tourette syndrome. Neurology *68*, 1979-1987. 10.1212/01.wnl.0000264417.18604.12.
29. Lee, J., Wang, W., and Sabatini, B.L. (2020). Anatomically segregated basal ganglia pathways allow parallel behavioral modulation. Nat Neurosci *23*, 1388-1398. 10.1038/s41593-020-00712-5.
30. Foster, N.N., Barry, J., Korobkova, L., Garcia, L., Gao, L., Becerra, M., Sherafat, Y., Peng, B., Li, X., Choi, J.H., et al. (2021). The mouse cortico-basal ganglia-thalamic network. Nature *598*, 188-194. 10.1038/s41586-021-03993-3.
31. McElvain, L.E., Chen, Y., Moore, J.D., Brigidi, G.S., Bloodgood, B.L., Lim, B.K., Costa, R.M., and Kleinfeld, D. (2021). Specific populations of basal ganglia output neurons target distinct brain stem areas while collateralizing throughout the diencephalon. Neuron *109*, 1721-1738.e1724. 10.1016/j.neuron.2021.03.017.
32. Aoki, S., Smith, J.B., Li, H., Yan, X., Igarashi, M., Coulon, P., Wickens, J.R., Ruigrok, T.J., and Jin, X. (2019). An open cortico-basal ganglia loop allows limbic control over motor output via the nigrothalamic pathway. Elife *8*. 10.7554/eLife.49995.
33. Hariz, M.I., and Robertson, M.M. (2010). Gilles de la Tourette syndrome and deep brain stimulation. Eur J Neurosci *32*, 1128-1134. 10.1111/j.1460-9568.2010.07415.x.
34. Arnts, H., Coolen, S.E., Fernandes, F.W., Schuurman, R., Krauss, J.K., Groenewegen, H.J., and van den Munckhof, P. (2023). The intralaminar thalamus: a review of its role as a target in functional neurosurgery. Brain Commun *5*, fcad003. 10.1093/braincomms/fcad003.
35. Manvich, D.F., Webster, K.A., Foster, S.L., Farrell, M.S., Ritchie, J.C., Porter, J.H., and Weinshenker, D. (2018). The DREADD agonist clozapine N-oxide (CNO) is reverse-metabolized to clozapine and produces clozapine-like interoceptive stimulus effects in rats and mice. Sci Rep *8*, 3840. 10.1038/s41598-018-22116-z.
36. Rodd, Z.A., Engleman, E.A., Truitt, W.A., Burke, A.R., Molosh, A.I., Bell, R.L., and Hauser, S.R. (2022). CNO Administration Increases Dopamine and Glutamate in the Medial Prefrontal Cortex of Wistar Rats: Further Concerns for the Validity of the CNO-activated DREADD Procedure. Neuroscience *491*, 176-184. 10.1016/j.neuroscience.2022.03.028.
37. Scharf, J.M., Yu, D., Mathews, C.A., Neale, B.M., Stewart, S.E., Fagerness, J.A., Evans, P.,

Gamazon, E., Edlund, C.K., Service, S.K., et al. (2013). Genome-wide association study of Tourette's syndrome. Mol Psychiatry *18*, 721-728. 10.1038/mp.2012.69.

38. Willsey, A.J., Fernandez, T.V., Yu, D., King, R.A., Dietrich, A., Xing, J., Sanders, S.J., Mandell, J.D., Huang, A.Y., Richer, P., et al. (2017). De Novo Coding Variants Are Strongly Associated with Tourette Disorder. Neuron *94*, 486-499.e489. 10.1016/j.neuron.2017.04.024.
39. Lu, Q., Zhou, Y., Qian, Q., Chen, Z., Tan, Q., Chen, H., Yin, F., Wang, Y., Liu, Z., Tian, P., and Sun, D. (2024). Whole-exome sequencing identifies high-confidence genes for tic disorders in a Chinese Han population. Clin Chim Acta *561*, 119759. 10.1016/j.cca.2024.119759.
40. Kowalski, T.F., Wang, R., and Tischfield, M.A. (2025). Genetic advances and translational phenotypes in rodent models for Tourette disorder. Curr Opin Neurobiol *90*, 102967. 10.1016/j.conb.2024.102967.
41. Godar, S.C., Mosher, L.J., Di Giovanni, G., and Bortolato, M. (2014). Animal models of tic disorders: a translational perspective. J Neurosci Methods *238*, 54-69. 10.1016/j.jneumeth.2014.09.008.
42. McCairn, K.W., Nagai, Y., Hori, Y., Ninomiya, T., Kikuchi, E., Lee, J.Y., Suhara, T., Iriki, A., Minamimoto, T., Takada, M., et al. (2016). A Primary Role for Nucleus Accumbens and Related Limbic Network in Vocal Tics. Neuron *89*, 300-307. 10.1016/j.neuron.2015.12.025.
43. Gittis, A.H., Berke, J.D., Bevan, M.D., Chan, C.S., Mallet, N., Morrow, M.M., and Schmidt, R. (2014). New roles for the external globus pallidus in basal ganglia circuits and behavior. J Neurosci *34*, 15178-15183. 10.1523/JNEUROSCI.3252-14.2014.
44. Matsumura, M., Tremblay, L., Richard, H., and Filion, M. (1995). Activity of pallidal neurons in the monkey during dyskinesia induced by injection of bicuculline in the external pallidum. Neuroscience *65*, 59-70. 10.1016/0306-4522(94)00484-m.
45. Grabli, D., McCairn, K., Hirsch, E.C., Agid, Y., Féger, J., François, C., and Tremblay, L. (2004). Behavioural disorders induced by external globus pallidus dysfunction in primates: I. Behavioural study. Brain *127*, 2039-2054. 10.1093/brain/awh220.
46. Bronfeld, M., Belelovsky, K., Erez, Y., Bugaysen, J., Korngreen, A., and Bar-Gad, I. (2010). Bicuculline-induced chorea manifests in focal rather than globalized abnormalities in the activation of the external and internal globus pallidus. J Neurophysiol *104*, 3261-3275. 10.1152/jn.00093.2010.
47. Tachibana, Y., Kita, H., Chiken, S., Takada, M., and Nambu, A. (2008). Motor cortical control of internal pallidal activity through glutamatergic and GABAergic inputs in awake monkeys. Eur J Neurosci *27*, 238-253. 10.1111/j.1460-9568.2007.05990.x.
48. McCairn, K.W., Iriki, A., and Isoda, M. (2013). Global dysrhythmia of cerebro-basal ganglia-cerebellar networks underlies motor tics following striatal disinhibition. J Neurosci *33*, 697-708. 10.1523/JNEUROSCI.4018-12.2013.

49. Murakami, J., Tachibana, Y., Akiyama, S., Kato, T., Taniguchi, A., Nakajima, Y., Shimoda, M., Wake, H., Kano, Y., Takada, M., et al. (2019). Oral splint ameliorates tic symptoms in patients with tourette syndrome. Mov Disord *34*, 1577-1578. 10.1002/mds.27819.
50. Yoshida, A., Fujio, T., Sato, F., Ali, M.S.S., Haque, T., Ohara, H., Moritani, M., Kato, T., Dostrovsky, J.O., and Tachibana, Y. (2017). Orofacial proprioceptive thalamus of the rat. Brain Struct Funct *222*, 2655-2669. 10.1007/s00429-016-1363-1.
51. Sato, F., Uemura, Y., Kanno, C., Tsutsumi, Y., Tomita, A., Oka, A., Kato, T., Uchino, K., Murakami, J., Haque, T., et al. (2017). Thalamo-insular pathway conveying orofacial muscle proprioception in the rat. Neuroscience *365*, 158-178. 10.1016/j.neuroscience.2017.09.050.
52. Craig, A.D. (2002). How do you feel? Interoception: the sense of the physiological condition of the body. Nat Rev Neurosci *3*, 655-666. 10.1038/nrn894.
53. Craig, A.D. (2009). How do you feel--now? The anterior insula and human awareness. Nat Rev Neurosci *10*, 59-70. 10.1038/nrn2555.
54. Namkung, H., Kim, S.H., and Sawa, A. (2017). The Insula: An Underestimated Brain Area in Clinical Neuroscience, Psychiatry, and Neurology. Trends Neurosci *40*, 200-207. 10.1016/j.tins.2017.02.002.
55. Lozano, A.M., Lang, A.E., Galvez-Jimenez, N., Miyasaki, J., Duff, J., Hutchinson, W.D., and Dostrovsky, J.O. (1995). Effect of GPi pallidotomy on motor function in Parkinson's disease. Lancet *346*, 1383-1387. 10.1016/s0140-6736(95)92404-3.
56. Lang, A.E., and Lozano, A.M. (1998). Parkinson's disease. First of two parts. N Engl J Med *339*, 1044-1053. 10.1056/NEJM199810083391506.
57. Obeso, J.A., Olanow, C.W., Rodriguez-Oroz, M.C., Krack, P., Kumar, R., Lang, A.E., and Group, D.-B.S.f.P.s.D.S. (2001). Deep-brain stimulation of the subthalamic nucleus or the pars interna of the globus pallidus in Parkinson's disease. N Engl J Med *345*, 956-963. 10.1056/NEJMoa000827.
58. Lozano, A.M., Lipsman, N., Bergman, H., Brown, P., Chabardes, S., Chang, J.W., Matthews, K., McIntyre, C.C., Schlaepfer, T.E., Schulder, M., et al. (2019). Deep brain stimulation: current challenges and future directions. Nat Rev Neurol *15*, 148-160. 10.1038/s41582-018-0128-2.
59. Vandewalle, V., van der Linden, C., Groenewegen, H.J., and Caemaert, J. (1999). Stereotactic treatment of Gilles de la Tourette syndrome by high frequency stimulation of thalamus. Lancet *353*, 724. 10.1016/s0140-6736(98)05964-9.
60. Singer, H.S. (2005). Tourette's syndrome: from behaviour to biology. Lancet Neurol *4*, 149-159. 10.1016/S1474-4422(05)01012-4.
61. Sadikot, A.F., and Rymar, V.V. (2009). The primate centromedian-parafascicular complex: anatomical organization with a note on neuromodulation. Brain Res Bull *78*, 122-130. 10.1016/j.brainresbull.2008.09.016.

62. Cover, K.K., and Mathur, B.N. (2021). Rostral Intralaminar Thalamus Engagement in Cognition and Behavior. Front Behav Neurosci *15*, 652764. 10.3389/fnbeh.2021.652764.

63. Alexander, G.E., DeLong, M.R., and Strick, P.L. (1986). Parallel organization of functionally segregated circuits linking basal ganglia and cortex. Annu Rev Neurosci *9*, 357-381. 10.1146/annurev.ne.09.030186.002041.

64. Alexander, G.E., and Crutcher, M.D. (1990). Functional architecture of basal ganglia circuits: neural substrates of parallel processing. Trends Neurosci *13*, 266-271. 10.1016/0166-2236(90)90107-l.

65. Tremblay, L., Worbe, Y., Thobois, S., Sgambato-Faure, V., and Féger, J. (2015). Selective dysfunction of basal ganglia subterritories: From movement to behavioral disorders. Mov Disord *30*, 1155-1170. 10.1002/mds.26199.

66. Gehrlach, D.A., Weiand, C., Gaitanos, T.N., Cho, E., Klein, A.S., Hennrich, A.A., Conzelmann, K.K., and Gogolla, N. (2020). A whole-brain connectivity map of mouse insular cortex. Elife *9*. 10.7554/eLife.55585.

67. Franklin, K.B.J., and Paxinos, G. (2008). The Mouse Brain in Stereotaxic Coordinates, Compact, 3rd Edition.

68. Mathis, A., Mamidanna, P., Cury, K.M., Abe, T., Murthy, V.N., Mathis, M.W., and Bethge, M. (2018). DeepLabCut: markerless pose estimation of user-defined body parts with deep learning. Nat Neurosci *21*, 1281-1289. 10.1038/s41593-018-0209-y.

69. Cantu, D.A., Wang, B., Gongwer, M.W., He, C.X., Goel, A., Suresh, A., Kourdougli, N., Arroyo, E.D., Zeiger, W., and Portera-Cailliau, C. (2020). EZcalcium: Open-Source Toolbox for Analysis of Calcium Imaging Data. Front Neural Circuits *14*, 25. 10.3389/fncir.2020.00025.

70. Okada, T., Kato, D., Nomura, Y., Obata, N., Quan, X., Morinaga, A., Yano, H., Guo, Z., Aoyama, Y., Tachibana, Y., et al. (2021). Pain induces stable, active microcircuits in the somatosensory cortex that provide a therapeutic target. Sci Adv *7*. 10.1126/sciadv.abd8261.

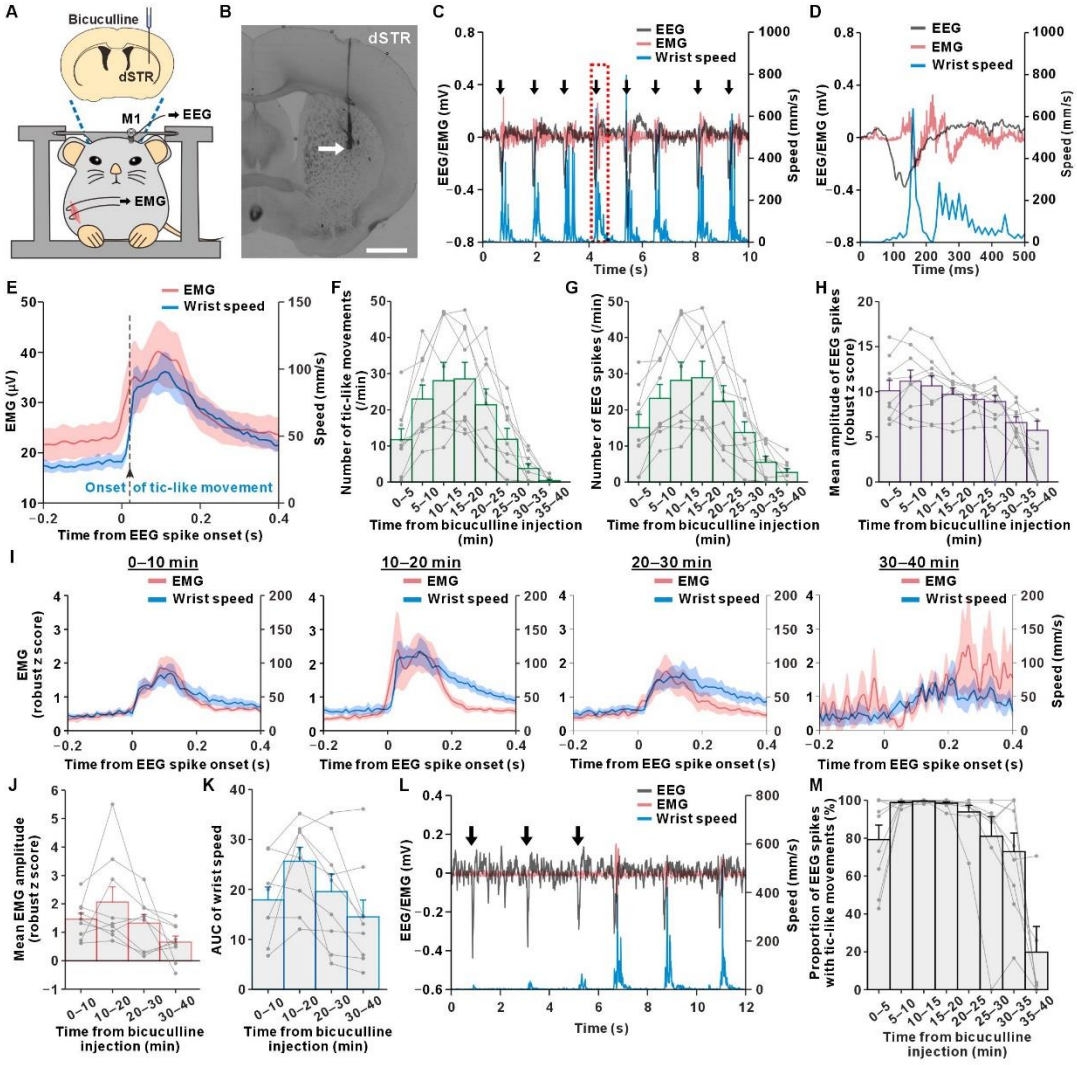

Fig. 1 Kuno et al.

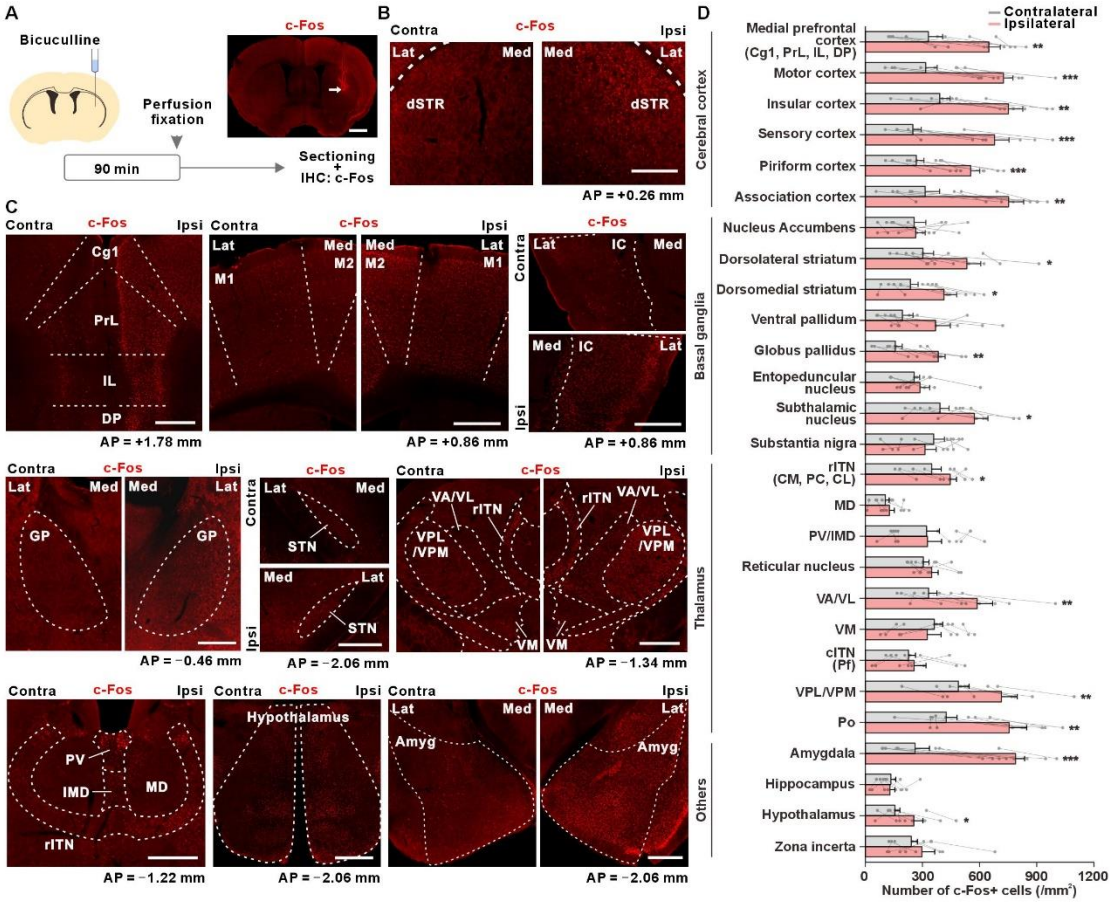

Fig. 2 Kuno et al.

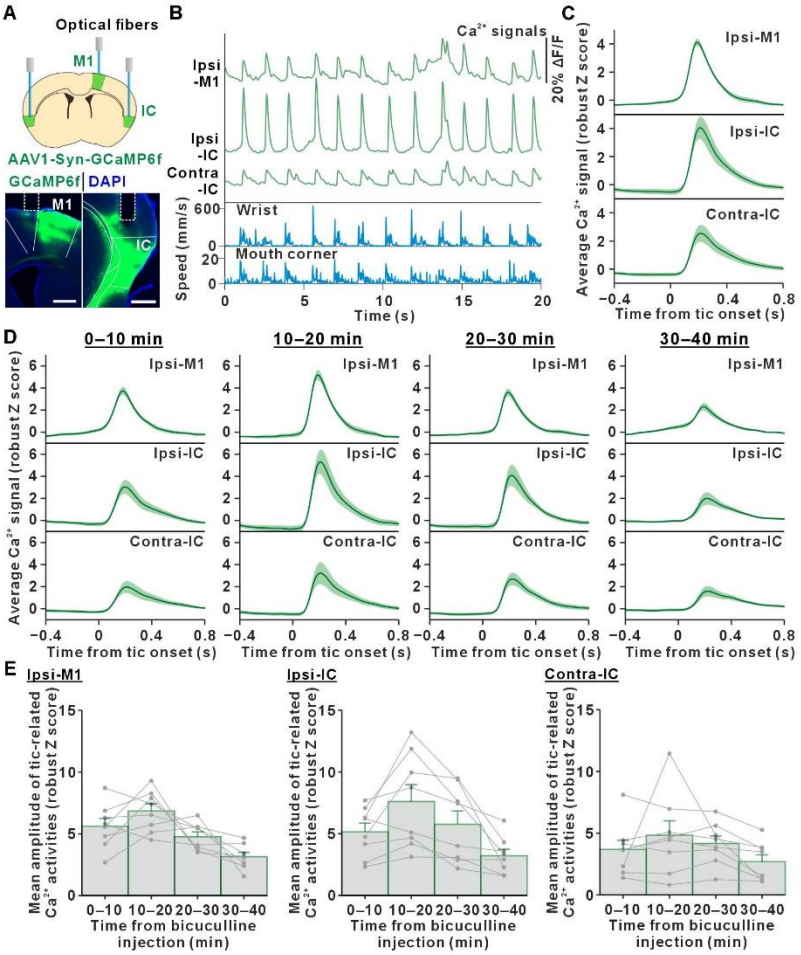

Fig. 3 Kuno et al.

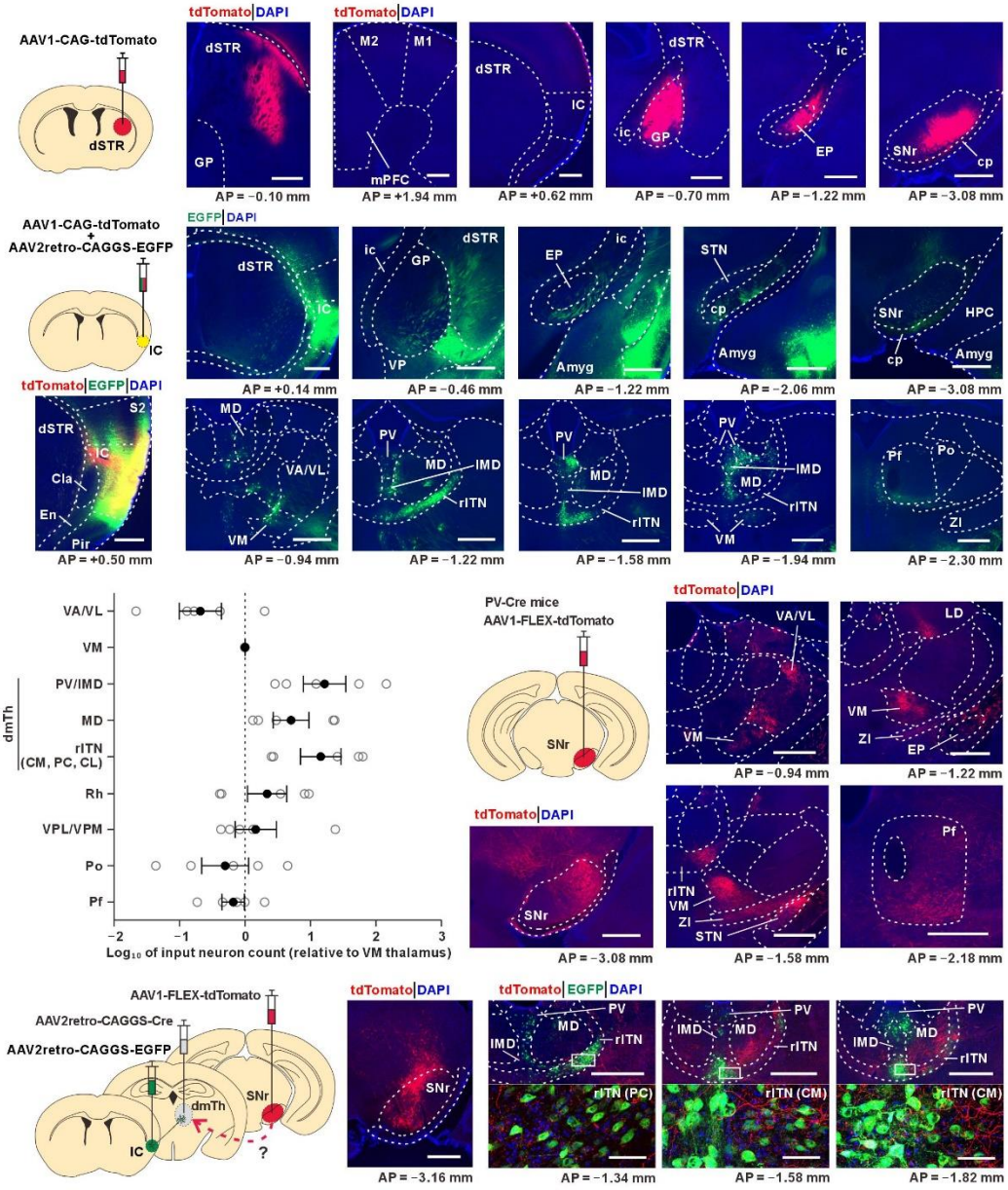

Fig. 4 Kuno et al.

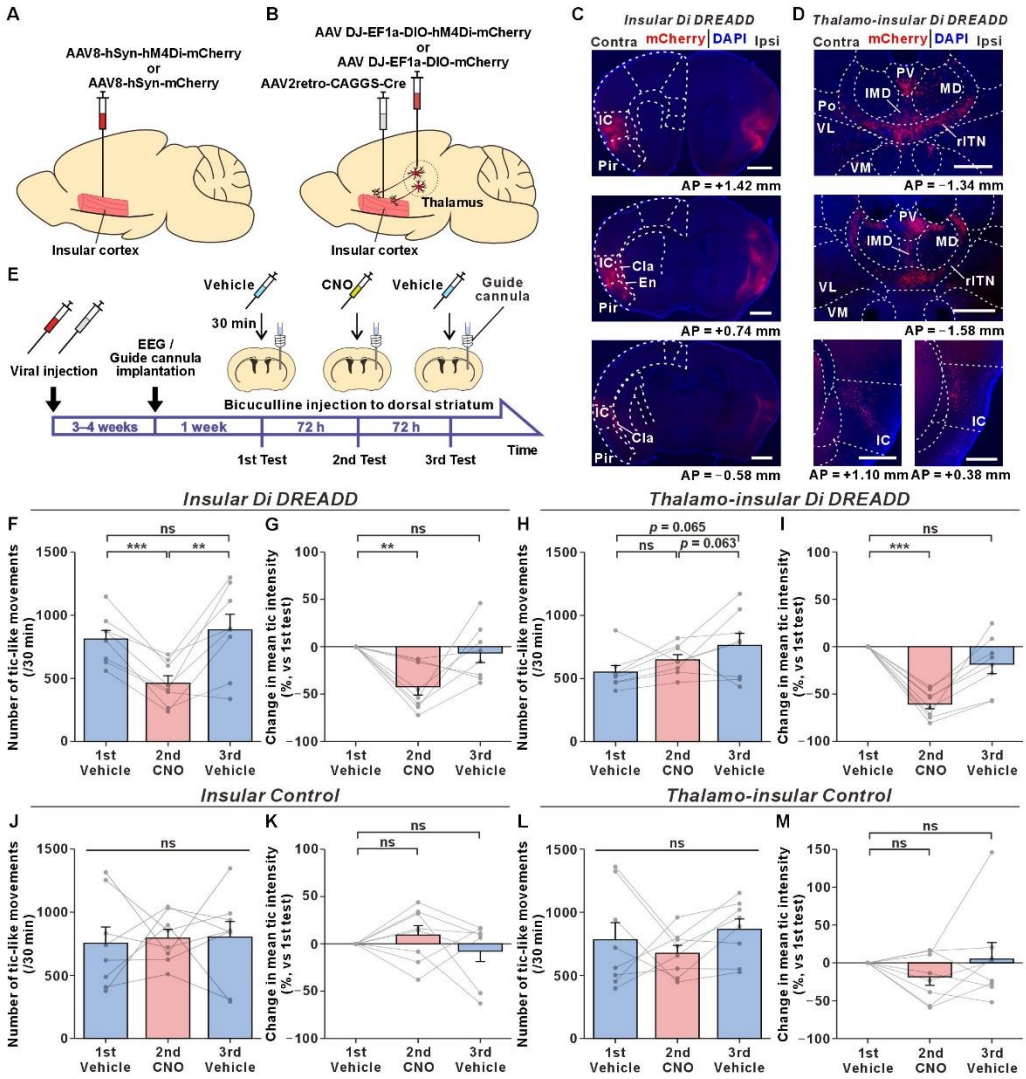

Fig. 5 Kuno et al.

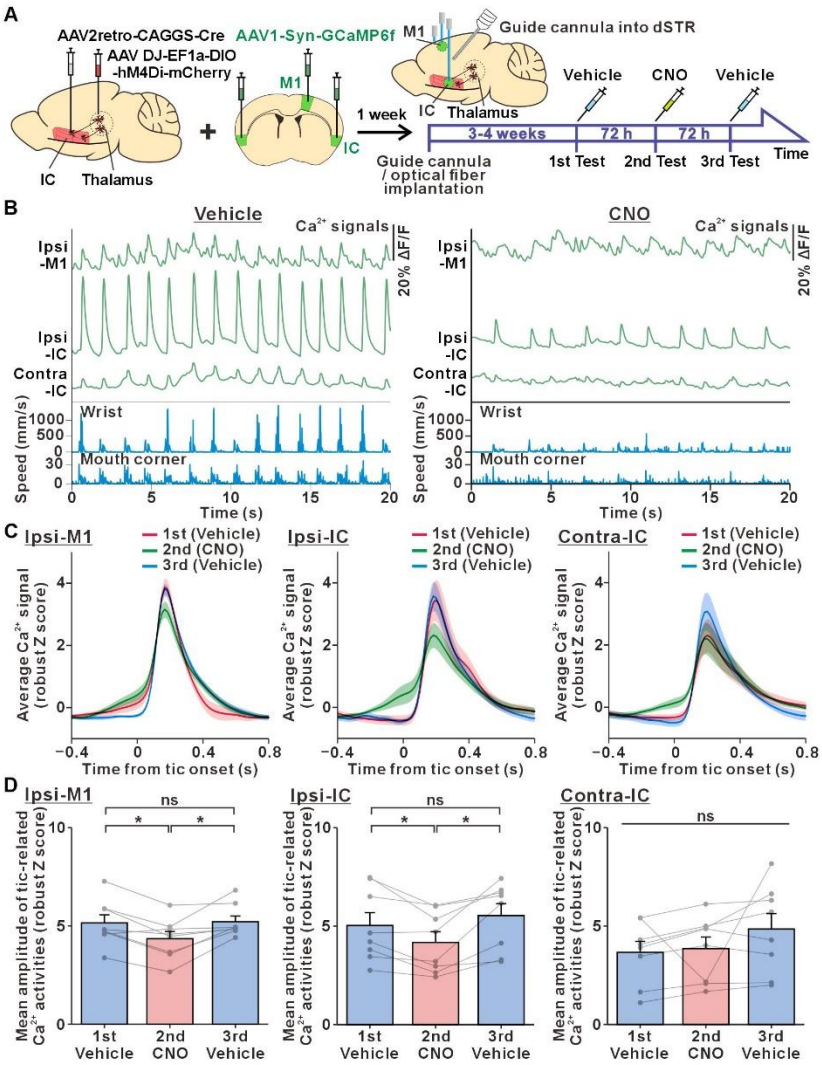

Fig. 6 Kuno et al.